PHYSICAL REVIEW C VOLUME 21, NUMBER 6 JUNE 1980

Angular distributions and ranges of heavy products from quasi-elastic transfer reactions induced by heavy ions in ^{209}Bi

D. Gardes, R. Bimbot, J. Maison, and M. F. Rivet
Laboratoire de Chimie Nucléaire, Institut de Physique Nucléaire, B.P. n° 1, 91406 Orsay, France

A. Fleury, F. Hubert, and Y. Llabador
Centre d'Etudes Nucléaires de Bordeaux Gradignan, Le Haut Vigneau, 33170 Gradignan, France

(Received 15 November 1979)

The projected ranges, angular distributions and range distributions at each laboratory angle have been measured for one-, two-, and three-proton transfer reactions induced in ^{209}Bi by various heavy ions from ^{14}N to ^{63}Cu. The products observed were ^{210}Po, ^{211}At, and ^{211}Rn. They were identified by their radioactive decay characteristics. Some complementary experiments have been performed using Tl and Au targets. The angular and energy distributions have been used to identify the most probable reaction paths leading to the observed isotopes. At low incident energy, these reaction paths appear to be those which correspond to the most favorable energetics, for all incident ions. At higher energies, more complex reaction channels have a significant contribution to the production of the observed isotopes. For all incident ions, the position of the angular distribution maximum θ_{max} is governed by the value of the ratio E/B of the incident energy to the interaction barrier. The variation of θ_{max} versus E/B is very similar to that of the rainbow angle corresponding to elastic scattering. This might indicate that quasi-elastic transfer and rainbow scattering occur for similar distances of closest approach between colliding nuclei.

[NUCLEAR REACTIONS ^{209}Bi(HI,x)^{210}Po, ^{211}At, ^{211}Rn, with HI=^{14}N, ^{16}O, ^{19}F, ^{40}Ar, ^{40}Ca, ^{56}Fe, and ^{63}Cu. Measured $\sigma(\theta)$, recoil ranges. Deduced most probable reaction path.]

I. INTRODUCTION

This work is part of a systematic study of quasi-elastic transfer reactions induced by heavy ions in heavy targets. This study is centered on the evolution of the reaction characteristics when the incident mass is increased. Absolute cross sections, projected ranges (on the beam axis), and angular and energy distributions of the heavy transfer residues have been determined using recoil techniques, associated with off-line activity measurements. Such techniques are particularly fruitful for this type of study in which large quantities of data must be gathered. The resolution obtained for the energy distributions is poorer than that associated with light transfer fragments (see for example Refs. 1–3 and the review papers[4,5]), so that it is not possible to separate final levels. But such a separation is not necessary for deriving the gross features of the reaction mechanisms. Moreover, the resolution obtained for angular distributions is generally sufficient, as these distributions exhibit a single peak for the systems and energies concerned here. Finally, the main advantage of these techniques is that the final product atomic numbers and masses are unambiguously identified.

The excitation functions have been measured for several products of transfer reactions induced in ^{209}Bi by 10 ions, from ^{12}C to ^{84}Kr. These data have been published in Refs. 6–8. The influence of energetics on the threshold of these reactions was discussed qualitatively in Ref. 9 and a quantitative interpretation was proposed in Ref. 10.

The present paper concerns projected ranges, angular and energy distributions. Projected range distributions have been measured at several energies for ^{210}Po, ^{211}At, and ^{211}Rn produced through transfer reactions induced in ^{209}Bi by ^{19}F, ^{40}Ar, ^{40}Ca, ^{56}Fe, and ^{63}Cu. Angular distributions, and range distributions at all laboratory angles have been measured for the same nuclei produced by ^{14}N, ^{16}O, ^{19}F, ^{40}Ar, and ^{40}Ca induced reactions in ^{209}Bi. Similar data concerning ^{12}C induced reactions in ^{209}Bi and ^{197}Au have been already published.[6]

As several reaction channels may in principle lead to the production of a given final nucleus, the angular and energy distributions have been used to gain better assignment of the transfer reactions involved in this production. In order to remove some ambiguities which remained after this kinematic analysis, a few complementary experiments have been performed. These experiments consisted in measuring the angular distributions or ranges of transfer products from reactions induced in Au and Tl targets. Moreover, for ^{40}Ar projectiles, the cross sections and angular distributions of light transfer residues (^{43}K, ^{41}Ar, ^{39}Cl, and ^{38}S) have been measured and the data

relative to ^{39}Cl and ^{38}S have been compared to those obtained for the complementary heavy products ^{210}Po and ^{211}At.

The experimental technique is described in Sec. II and the experimental results are given in Sec. III. The identification of the reactions leading to the observed nuclei is presented in Sec. IV, and the main features of the c.m. angular distributions and of the variation of projected ranges with incident energy are discussed in Sec. V. The experimental angular distributions presented here have been used as a basis for a quantitative interpretation using a formalism derived from the distorted-wave Born approximation (DWBA). This interpretation was published in Ref. 11.

II. EXPERIMENTAL TECHNIQUES

The experimental technique consisted of irradiations followed by off-line activity measurements.

A. Projectiles and targets

Beams of ^{14}N, ^{16}O, ^{19}F, ^{40}Ar, ^{40}Ca, ^{56}Fe, and ^{63}Cu were accelerated by the Orsay Alice facility. The incident energy was determined from the cyclotron frequency and extraction radius, and a small correction was applied to take into account the systematic deviation observed[12] between calculated and measured energies. It has been shown[12] that such a procedure leads to uncertainties of the order of ±2.5% on the energy. The low-energy ^{19}F experiments ($E < 110$ MeV) were performed using the Orsay Tandem MP Van de Graaff accelerator. For these experiments, the energy was measured with an accuracy better than ±0.1% using a calibrated magnet.

Targets of Bi, Au, and natural Tl were prepared by evaporation onto aluminum backings. The target thicknesses ranged from 50 μg/cm^2 (for the angular distributions corresponding to light projectiles) to 1 mg/cm^2 (for the projected range measurements relative to heavy projectiles).

B. Experimental devices

The projected ranges were measured simultaneously with the absolute cross sections published in Ref. 8; the target and a stack of Al catcher foils were placed in a Faraday cup [see Fig. 1(a)]. After irradiation, the catcher foils were separated and their α activity was measured in 2π ionization chambers. The projected ranges were deduced from these measurements by the method described in Ref. 13. The only improvement relative to this method concerned the correction for α self-absorption in the catcher foils. In Ref. 13, this correction was made under the assumption

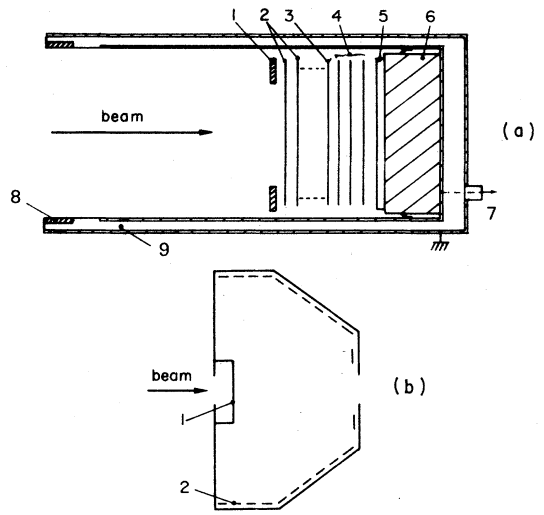

FIG. 1. Experimental set up. (a) For projected range measurements: (1) Al ring holding the stacks of foils on the Cu block. (2) Al degraders. (3) Target. (4) Al catcher foils. (5) Thick Al foil to stop all light reaction products. (6) Cu block. (7) Collected charges to beam integrator. (8) Ring shield. (9) Insulator. (b) Collection chamber: (1) Target. (2) Stacks of annular Al catcher foils.

that for each catcher foil, all the activity was concentrated in the mid-plane of the foil (i.e., at a depth $d = e/2$, e being the catcher foil thickness). In the present work the distribution of the activity along the d axis was taken into account. This distribution was obtained from an approximate determination of the range distribution without self-absorption correction. However, this improvement led to very small changes in the projected ranges. The range straggling ρ was deduced from the full width at half maximum (FWHM) W of the projected range distribution by the relation

$$\rho = \frac{W}{2.354 R_0} \tag{1}$$

in which R_0 is the average projected range (see Ref. 14).

For angular distribution measurements, the target was placed in the center of a collection chamber, and the recoil nuclei were stopped in angular catcher foils as indicated in Fig. 1(b). The target was placed either perpendicular to the beam or at 45°, according to the expected position of the angular distribution maximum. For light projectiles (up to ^{19}F), the experimental conditions were the same as in Ref. 6, while for the heaviest ions (^{40}Ar, ^{40}Ca), the conditions were similar to those of Ref. 15.

The technique used for measuring the recoil ranges at each laboratory angle depended on the

incident ion. For heavy projectiles, i.e., for large range values (>1 mg/cm^2 of Al), stacks of annular catcher foils were placed at each angle θ, and the range $R(\theta)$ was determined in the same way as the projected ranges.[15] For light projectiles, i.e., for low range values, thick annular catcher foils were used, and the recoil range (the depth of the α-emitting nucleus) was deduced from the energy degradation of the emitted α particle. This technique, also used in Ref. 6, is described in Ref. 16.

Finally, special systems were designed to collect simultaneously the light and heavy products of the transfer reactions at incident energies close to the interaction barrier. (See Fig. 2.) In Fig. 2(a) is shown the device which was used to measure the angular distribution of products for incident energies of 203 and 212 MeV. At the highest of these energies, the angular distributions of ^{210}Po and ^{211}At were measured from 10 to 60° using stacks of Al catcher foils. Simultaneously, the distributions of the light transfer products ^{38}S, ^{39}Cl, ^{41}Ar, and ^{43}K were measured from 60 to 120° using 10μ Au catcher foils. The choice of this material of high atomic number was made in order to reduce the contribution of spurious reactions induced by the scattered beam in the catcher foils. At 203 MeV, the angular interval corresponding to the heavy product distribution was the same, but the light products were collected in the angular interval 90–150°. In this experiment, the activity was lower, and the angular distributions could only be measured (with a sufficient accuracy) for the residual nuclei ^{210}Po, ^{211}At, and ^{41}Ar. The relative yields of light and heavy products were also derived from these experiments at 212 and 203 MeV.

Two other experiments were performed to measure the cross sections for these light and heavy products. A much smaller collection chamber was then used [see Fig. 2(b)]. The incident energies of 190 and 194 MeV were such that the heavy transfer products were emitted at forward angles and the light ones at backward angles ($\theta_{lab} > 90°$). The walls of the collection chamber were covered with Al catcher foils in the forward hemisphere and with Au catcher foils in the backward hemisphere.

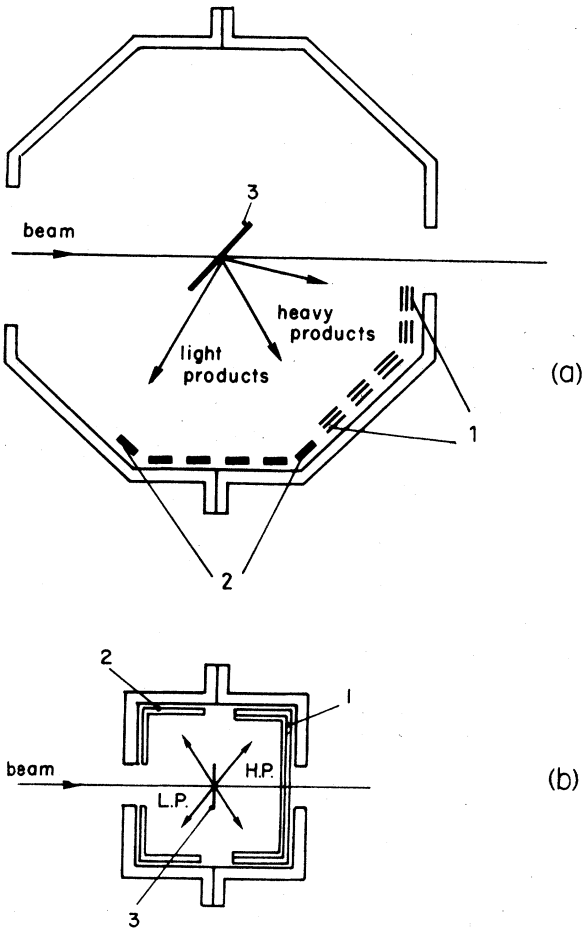

FIG. 2. Systems used for simultaneous collection of the light and heavy products. (a) For angular distribution measurements. (b) For cross section measurements. Both systems have cylindrical symmetry around the beam axis: (1) Al stacks of catcher foils for heavy products (HP). (2) Au thick catcher foils for light products (LP). (3) Target.

The activity caught by each hemisphere was counted as a whole, and the collection yield was assumed to be equal to 100%. The cross sections were thus measured relative to that of ^{211}At, as in the experiments at 212 and 203 MeV mentioned above. For each incident energy, the absolute cross sections for ^{211}At were measured in separate

TABLE I. Decay characteristics of the light products of Ar induced transfer reactions (from Ref. 18).

Isotope	Half-life	Decay mode	E_γ (keV)	Branching ratio
^{38}S	2.83 h	β^-	1942	0.84 ±0.02
^{39}Cl	56.2 min	β^-	250	0.47 ±0.02
			1267	0.543 ±0.013
			1517	0.385 ±0.012
^{41}Ar	1.83 h	β^-	1293	0.9922 ±0.0002
^{43}K	22.2 h	β^-	373	0.87 ±0.03

experiments in which the target was placed in the Faraday cup, as in Fig. 1(a).

C. Off-line measurements

The radionuclides were identified by their decay characteristics. These characteristics are given in Ref. 8 for heavy products and in Table I for the light ones. The activity measurements were performed using 2π ionization chambers for α spectrometry and Ge-Li detectors for γ spectrometry. The decay curves were analyzed by the least square fit method to determine the initial activity of each isotope. Details concerning the α-decay curve analysis can be found in Ref. 13.

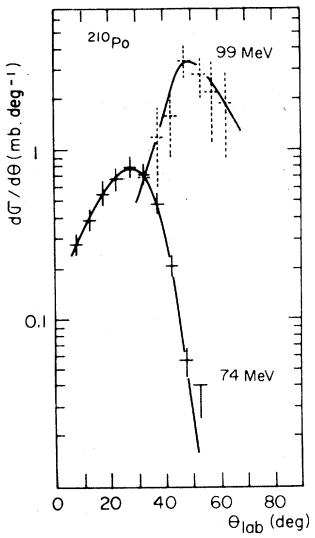

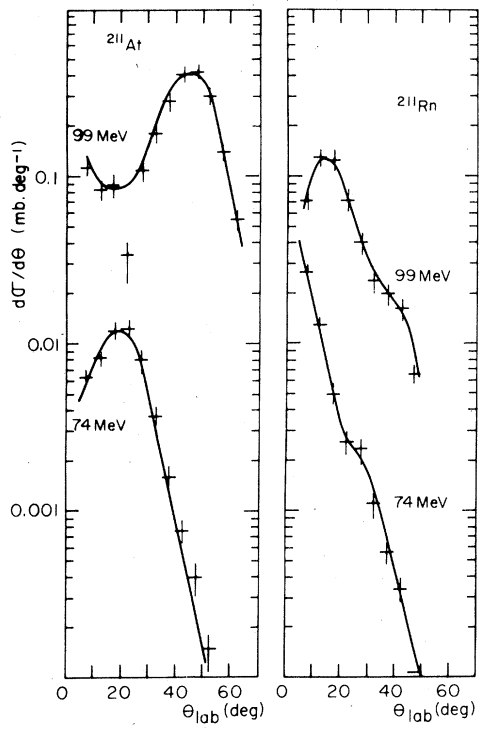

FIG. 3. Angular distributions of ^{210}Po, ^{211}At, and ^{211}Rn produced through ^{14}N + ^{209}Bi reactions at 74 and 99 MeV. The lines are drawn to guide the eye through the experimental points.

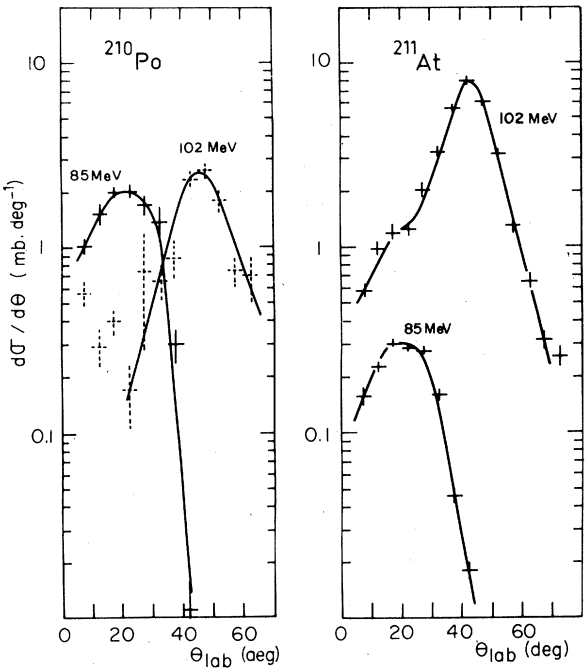

FIG. 4. Angular distributions of ^{210}Po and ^{211}At produced through ^{16}O + ^{209}Bi reactions at 85 and 102 MeV. The lines are drawn to guide the eye through the experimental points.

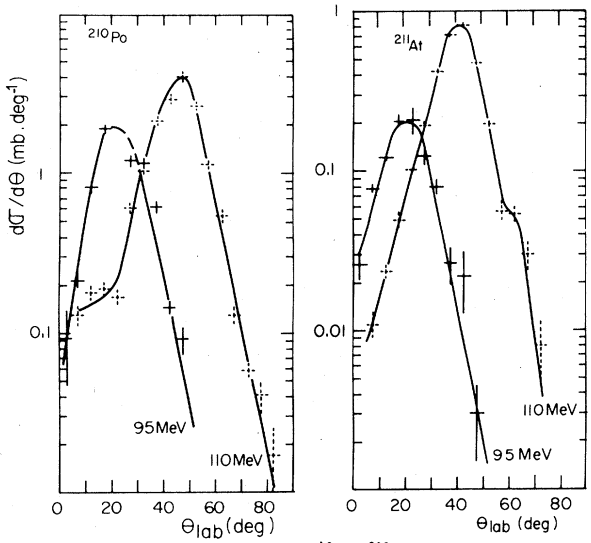

FIG. 5. Same as Fig. 4 for ^{19}F + ^{209}Bi reactions at 95 and 110 MeV.

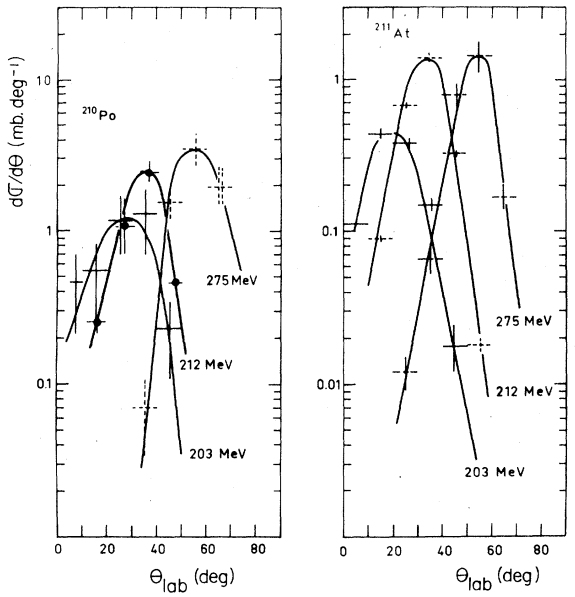

FIG. 6. Same as Fig. 4 for ^{40}Ar + ^{209}Bi reactions at 203, 212, and 275 MeV.

III. EXPERIMENTAL RESULTS

A. Angular distributions and ranges of heavy products in the laboratory system

The angular distributions obtained in the laboratory system for the nuclides ^{210}Po, ^{211}At, and ^{211}Rn produced through ^{14}N to ^{40}Ca induced reactions in ^{209}Bi are given in Figs. 3–7. Those obtained for the reactions ^{16}O + ^{197}Au → ^{198}Tl, ^{200}Tl, ^{204}Bi at the incident energy E_{lab} = 112 MeV are given in Fig. 8. Finally, the angular distribution corresponding to the reaction ^{40}Ar + ^{nat}Tl → ^{211}At at 242 MeV is given in Fig. 9.

Two remarks concerning these angular distributions can be made.

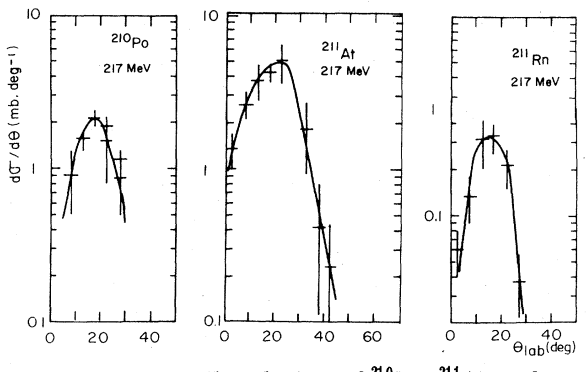

FIG. 7. Angular distributions of ^{210}Po, ^{211}At, and ^{211}Rn produced through ^{40}Ca + ^{209}Bi at 217 MeV. The lines are drawn to guide the eye through the experimental points.

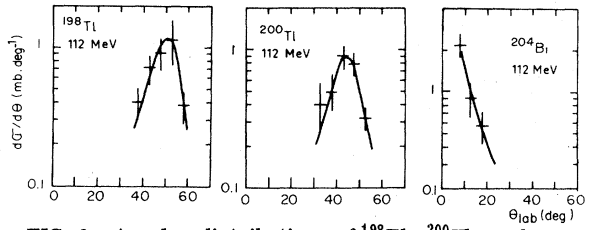

FIG. 8. Angular distributions of ^{198}Tl, ^{200}Tl, and ^{204}Bi produced through ^{16}O + ^{197}Au reactions at 112 MeV. The lines are drawn to guide the eye through the experimental points.

First it should be noted that all of them exhibit a pronounced side peaking, except for the reactions

$$^{14}\mathrm{N} + {}^{209}\mathrm{Bi} \rightarrow {}^{211}\mathrm{Rn} \text{ at } 74 \text{ MeV}, \tag{2}$$

and

$$^{16}\mathrm{O} + {}^{197}\mathrm{Au} \rightarrow {}^{204}\mathrm{Bi} \text{ at } 112 \text{ MeV} \tag{3}$$

for which a forward peaking is observed. Such a forward peaking is typical of a compound nucleus process.[6,17]

Therefore, from these angular distributions and the known parent-daughter relationships,[18] one can assign the productions of ^{211}Rn and ^{204}Bi to the following reactions:

$$^{14}\mathrm{N} + {}^{209}\mathrm{Bi} \rightarrow 4n + {}^{219}\mathrm{Th} \xrightarrow{\alpha \text{ decay}} {}^{215}\mathrm{Ra} \xrightarrow{\alpha \text{ decay}} {}^{211}\mathrm{Rn}, \tag{2'}$$

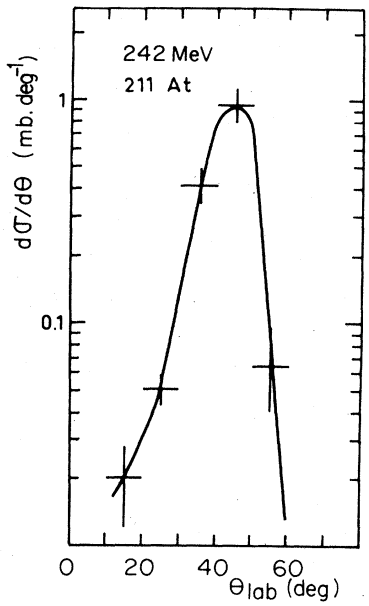

FIG. 9. Angular distribution of ^{211}At produced through the reaction ^{40}Ar + ^{nat}Tl → ^{211}At at E_{lab} = 242 MeV. The line is drawn to guide the eye.

$$^{16}O + ^{197}Au \rightarrow 5n + ^{208}Fr \xrightarrow{\alpha\ \text{decay}} ^{204}At \xrightarrow{\text{E.C.}} ^{204}Po \xrightarrow{\text{E.C.}} ^{204}Bi \quad (3')$$

(the symbol E.C. denotes electron capture decay).

The intermediate nuclei were not observed because of their short half-lives (^{215}Ra, ^{204}At) or small α branching ratio (^{204}Po).

This assignment is confirmed by the range measurements, and by the excitation energies calculated for the compound nuclei ^{223}Th ($E^* = 35$ MeV) and ^{213}Fr ($E^* = 71$ MeV) at the energies considered. Note that the excitation energy of 71 MeV is also consistent with the hypothesis of $(\alpha, 5n)$ evaporation. This would lead to the direct production of ^{204}At, which is not excluded by the angular distribution.

The second remark concerns the angle θ_{max} which corresponds to the maximum of the angular distributions. For a given projectile, this angle seems to depend mainly on the incident energy and to be independent of the transfer reaction. In order to compare the data corresponding to different projectiles, the value θ_{max} has been plotted versus the ratio E/B of the incident energy to the strong interaction barrier (calculated according to Ref. 19).

This plot, in which the results from Ref. 6 have been included, is shown in Fig. 10. The data have been divided into two groups according to the value of the ratio a/A_p of the transferred mass to the projectile mass. (The transferred mass a is known from the analysis described in Sec. IV.) For the data corresponding to $a/A_p < 0.2$, shown in Fig. 10(a), a strong correlation is observed between the value of θ_{max} and the ratio E/B. It will be shown in Sec. IV that this correlation may be related to the rainbow effect; the dotted line in Fig. 10(a) represents the variation of the rainbow angle, calculated for elastic scattering (See Sec. IV). This curve is independent of the system projectile target. From a phenomenological point of view, the correlation shown in Fig. 10(a) can be used to predict the position of the angular distribution maximum, in the laboratory system, for the heavy products of transfer reactions. Such predictions can be useful, either for isotope production purposes or for the identification of a reaction mechanism.

When the ratio a/A_p is larger than 0.2, the above mentioned correlation if no longer observed, as can be seen in Fig. 10(b). Moreover, the deviation from the position predicted by the systematics increases with the ratio a/A_p; this ratio is indicated for most of the points in Fig. 10(b). This property was used in Ref. 10 to distinguish between two-charge and four-charge transfers induced by ^{12}C in ^{209}Bi, both of these transfers leading finally to ^{211}At. This distinction was made by a comparison with the angular distributions relative to the same reactions for a gold target, which produced Tl and Bi isotopes, respectively. For both targets, the values of θ_{max} associated with two-charge transfers ($a/A_p = 0.25$–0.3) were about 35°, while those associated with four-charge transfers ($a/A_p = 0.67$) were found near 17.5°.

Note that the angular distribution measured for the reaction $^{40}Ar + ^{205}Tl \rightarrow ^{211}At$, which corresponds

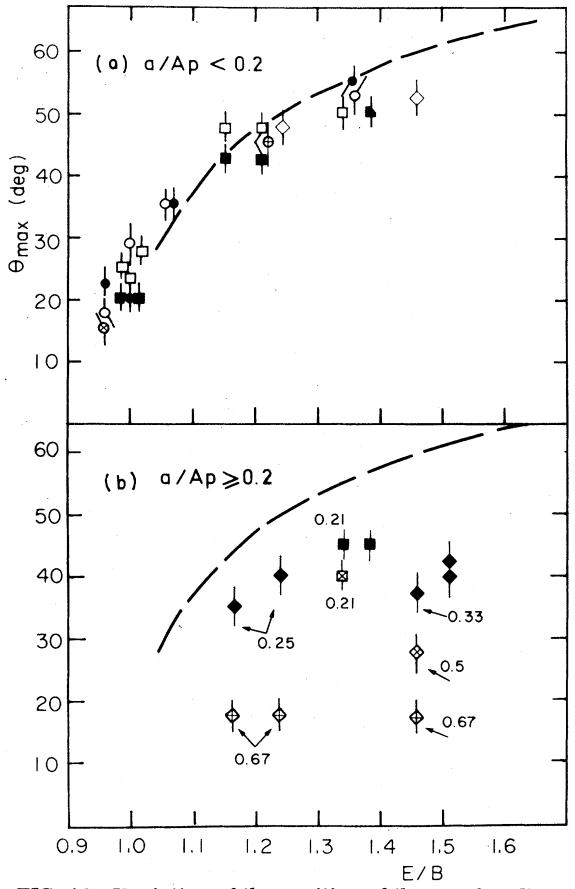

FIG. 10. Variation of the position of the angular distribution maximum θ_{max} (laboratory system) versus the ratio E/B. The shape of the symbols, which represent the experimental data, depend on the projectile: diamonds for ^{12}C, squares for ^{14}N, ^{16}O, ^{19}F, and circles for ^{40}Ar and ^{40}Ca. Open symbols represent single-proton transfer, black symbols two-charge transfer, and the symbols X and + inside circles, squares, or diamonds represent, respectively, three- and four-charge transfers. The dotted line represents the variation of the rainbow angle, calculated for elastic scattering. (a) For $a/A_p < 0.2$ a strong correlation between θ_{max} and E/B is observed, and the angle θ_{max} is close to the rainbow angle. (b) For $a/A_p \geq 0.2$, the deviation from the rainbow angle increases with increasing a/A_p. (The values of this ratio, when known, are indicated close to each point.)

TABLE II. Experimental values for the range R_0 and range straggling ρ measured at given angles in the laboratory system for ^{210}Po recoil nuclei in Al. The uncertainties in ρ values are of about ±15%. The recoil energy E_0 and energy straggling ρ_E are derived from R_0 and ρ as indicated in text.

Incident ion	Energy E_{lab} (MeV)	Angle θ_{lab} (deg)	Range R_0 (mg/cm^2)	R straggling ρ	Recoil energy E_0 (MeV)	E straggling ρ_E
^{14}N	74	5	0.79±0.04	0.17	13.3±1.2	<0.05
		15	0.83±0.04	0.16	14.2±1.2	<0.05
		25	0.77±0.04	0.13	12.8±1.1	<0.05
		35	0.67±0.03	0.12	10.8±1	<0.05
		45	0.57±0.03	0.18	9 ±0.8	<0.05
	99	17.5	0.43±0.04	0.24	6.7±0.6	<0.05
		35	0.41±0.04	0.30	6.5±0.6	0.17
		45	0.35±0.04	0.33	5.5±0.5	0.22
^{16}O	83	5	1.05±0.05	0.09	19 ±2	<0.05
		15	1.03±0.05	0.11	18.5±2	0.06
		25	0.96±0.05	0.09	17 ±1.7	<0.05
		35	0.83±0.05	0.19	14 ±1.6	0.19
	102	17.5	0.46±0.05		7.2±0.7	
		25	0.64±0.06	0.29	10.3±0.9	0.14
		35	0.67±0.06	0.29	11 ±1	0.14
		45	0.55±0.06	0.22	8.7±0.9	<0.05
		55	0.44±0.04	0.4	7 ±0.6	0.3

to a four-charge transfer, exhibits a maximum at 45°, in good agreement with the systematics of Fig. 10(a). This indicates that the relevant parameter for this classification is the ratio a/A_p (or the corresponding charge ratio z/Z_p), and not the absolute number of transferred nucleons (charges); here $a/A_p = 0.15-0.20$.

The data concerning the range values at each angle θ_{lab} are summarized in Tables II and III. In these tables, the values measured for the mean range R_0 and the range straggling parameter ρ [defined in Ref. 14 by Eq. (1)] are given for each projectile, energy, and laboratory angle. The mean recoil energy E_0, also given in Tables II and III, is deduced from R_0 using a range energy relationship, the low-energy part of which is represented in Fig. 11 by the solid line. This curve has been obtained from the experimental data[16,20-22] available at low energies, and the calculated values of Northcliffe and Schilling[23] at high energy.

In the last column of Tables II and III, the energy straggling parameter ρ_E is given. This parameter is deduced from ρ, as in Refs. 6 and 16, by subtracting from the range straggling the contributions of the straggling due to the slowing down process itself to the neutron evaporation and to the target thickness.

These data (angular distribution, recoil energy, and energy straggling) will be used to get the angular and energy distributions in the c.m. system, and to discuss the reaction paths leading to the observed nuclei (see Sec. IV).

B. Projected ranges

The ranges projected on the beam axis and range straggling values measured for the reactions induced by ^{19}F, ^{40}Ar, ^{40}Ca, ^{56}Fe, and ^{63}Cu are given in Tables IV–IX. Some of the data relative to ^{40}Ar projectiles had been already published,[13] but since that time small corrections were applied to the incident energies and to the projected range values, as indicated in Sec. II.

It can be seen from these tables that no significant difference is observed between the ranges and range stragglings corresponding to different reactions for a given projectile and energy. The variation of the projected range $R_{\parallel}$ of ^{211}At versus incident energy is shown in Fig. 12 for ^{40}Ca projectiles, as the most significant example.

The projected range increases slightly at low energy, then decreases sharply at high energy. The excitation function from Ref. 8 is shown on the same graph. It can be seen that the projected ranges begin to decrease when the cross sections reach the value corresponding to the plateau. This happens for an incident energy (E_0) 15 MeV

TABLE III. Same as Table II, but for ^{211}At recoil nuclei.

Incident ion	Energy E_{lab} (MeV)	Angle θ_{lab} (deg)	Range R_0 (mg/cm^2)	R straggling ρ	Recoil energy E_0 (MeV)	E straggling ρ_E
^{14}N	74	5	0.78 ± 0.04	0.12	13 ± 1.3	<0.05
		15	0.78 ± 0.04	0.14	13 ± 1.3	<0.05
		25	0.71 ± 0.04	0.10	12 ± 1.2	<0.05
	99	17.5	0.34 ± 0.02	0.31	5.2 ± 0.5	0.24
		25	0.29 ± 0.02	0.32	4.3 ± 0.4	0.24
		35	0.32 ± 0.02	0.41	5.0 ± 0.5	0.37
		45	0.29 ± 0.02	0.45	4.3 ± 0.4	0.40
^{16}O	83	5	1.06 ± 0.06	0.07	19.5 ± 2	0.06
		15	1.05 ± 0.06	0.10	19.4 ± 2	0.09
		25	0.93 ± 0.05	0.11	16 ± 1.7	0.07
		35	0.83 ± 0.04	0.17	14 ± 1.4	0.15
	102	7.5	0.35 ± 0.02	0.33	5.3 ± 0.5	0.22
		17.5	0.41 ± 0.03	0.60	7.2 ± 0.7	0.57
		25	0.64 ± 0.04	0.42	10 ± 1	0.37
		35	0.57 ± 0.04	0.30	9.4 ± 0.9	0.22
		45	0.49 ± 0.03	0.28	7.7 ± 0.8	0.16
		55	0.42 ± 0.03	0.30	6.7 ± 0.7	0.21
^{19}F	95	2.5	1.43 ± 0.1	0.34	30 ± 3	0.09
		7.5	1.25 ± 0.09	0.15	25 ± 3	<0.05
		12.5	1.26 ± 0.09	0.22	25 ± 3	<0.05
		17.5	1.20 ± 0.09		23.5 ± 2.5	
		27.5	1.17 ± 0.09	0.29	22.5 ± 3	<0.05
		37.5	0.84 ± 0.08	0.17	15 ± 2	<0.05
		42.5	0.93 ± 0.08		17 ± 2	
	110	22.5	0.78 ± 0.12	0.30	14 ± 3	0.17
		27.5	0.89 ± 0.13	0.14	16 ± 3	<0.05
		32.5	0.76 ± 0.12	0.15	13 ± 2.6	<0.05
		37.5	0.76 ± 0.12	0.18	13 ± 2.6	<0.05
		42.5	0.71 ± 0.10	0.11	12.5 ± 2.5	<0.05
		47.5	0.58 ± 0.08	0.16	10 ± 2	<0.05
		52.5	0.56 ± 0.08	0.21	9 ± 1.8	<0.05
^{40}Ar	203	7.5	3.4 ± 0.3	0.14	110 ± 14	<0.05
		15	3.1 ± 0.3	0.10	95 ± 12	<0.05
		25	2.9 ± 0.3	0.08	86 ± 11	<0.05
		35	2.7 ± 0.3	0.11	75 ± 10	<0.05
		45	2.1 ± 0.2	0.15	53 ± 7	<0.05
	212	5	3.1 ± 0.3	0.10	95 ± 12	<0.05
		15	2.9 ± 0.3	0.16	86 ± 10	<0.05
		25	2.8 ± 0.3	0.14	80 ± 9	<0.05
		35	2.6 ± 0.3	0.16	70 ± 14	<0.05
		45	2.5 ± 0.3	0.27	65 ± 13	0.1
	275	45	1.53 ± 0.08	0.25	32 ± 4	0.23
		55	1.55 ± 0.10	0.21	33 ± 4	0.18
		65	1.59 ± 0.12	0.24	34 ± 4	0.22
^{40}Ca	217	2.5	3.4 ± 0.3	0.11	110 ± 10	<0.05
		7.5	3.1 ± 0.3	0.15	95 ± 10	<0.05
		12.5	2.95 ± 0.3	0.13	88 ± 9	<0.05
		17.5	2.9 ± 0.3	0.15	86 ± 10	<0.05
		22.5	2.95 ± 0.3	0.17	88 ± 10	<0.05

TABLE III. *(Continued.)*

Incident ion	Energy E_{lab} (MeV)	Angle θ_{lab} (deg)	Range R_0 (mg/cm^2)	R straggling ρ	Recoil energy E_0 (MeV)	E straggling ρ_E
		27.5	2.7 ±0.3	0.13	75 ± 8	<0.05
		35	2.6 ±0.7	0.30	70 ±20	0.17
		45	2.5 ±0.8	0.36	65 ±25	0.26

lower than the strong interaction barrier B, calculated according to Ref. 9, for the $^{40}Ca + ^{209}Bi$ reaction. One should note, however, that this energy E_0 is approximately equal to the barrier B_v which corresponds to the systematics of Vaz and Alexander[24] (i.e., a Coulomb barrier calculated with a radius parameter r_e equal to 1.43 fm for the system considered). This seems to indicate that the use of this systematics leads to a better estimation of the strong interaction barrier than the calculation of Ref. 19 based on the energy density formalism. The decreasing behavior of projected ranges when plotted against incident energy has been observed several times[6,7,13,20,22,25,26] and is considered as typical of transfer reactions. It differs strongly from the variation expected under the assumption of a compound nucleus process (curve labeled C.N. in Fig. 12), but the increasing part of the curve $R=f(E_{lab})$ at low energy had never been observed before. This observation was possible here because of the high cross sections observed near the barrier for this reaction. Such high cross sections can be explained by a favorable energy balance for the reaction $^{40}Ca + ^{209}Bi \rightarrow ^{211}At$ (see Refs. 8 and 9).

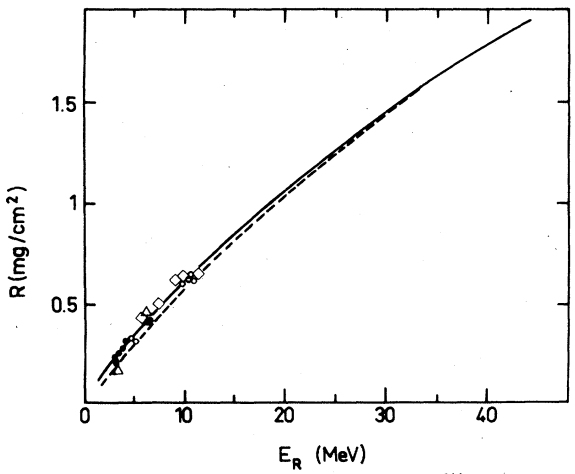

FIG. 11. Range energy relationship for ^{211}At nuclei in Al. The experimental values are represented by the following symbols: triangles (Ref. 20), squares (Ref. 21), open circles (Ref. 22), and black circles (Ref. 16). The dotted line represents the calculated values from Ref. 23, and the solid line the relationship adopted here.

The variation of the projected ranges versus E_{lab} are shown in Fig. 13 for the ions ^{19}F, ^{40}Ar, ^{56}Fe, and ^{63}Cu. These curves are similar to that observed for the ^{40}Ca induced reaction which is presented again in Fig. 13 for comparison, but the low-energy increase is less clear. Only a constant value of $R_{\parallel}$ is observed at low energy for projectiles other than ^{40}Ca. This behavior of the projected ranges versus incident energy will be discussed in Sec. V.

C. Light and heavy transfer products from Ar induced reactions

Angular distributions. The laboratory distributions of ^{38}S, ^{39}Cl, ^{41}Ar, and ^{43}K produced in the reaction $^{40}Ar + ^{209}Bi$ at 212 MeV are given in Fig. 14, together with that of ^{41}Ar obtained at 203 MeV. The heavy product distributions at the same energies have been given in Sec. III A. For $E_{lab}=212$ MeV, one can observe in Fig. 14 that the position of the angular distribution maximum is approximately the same for the four reactions considered ($\theta_{max}=88\pm5°$). This property was already outlined for the heavy products. The complementary aspect of the distributions relative to ^{38}S and ^{39}Cl

TABLE IV. Experimental projected ranges $R_{\parallel}$ and range straggling ρ for ^{210}Po, and ^{211}At produced through $^{19}F + ^{209}Bi$ reactions. The uncertainties in ρ values are of about ±15%.

	^{210}Po		^{211}At	
^{19}F E_{lab} (MeV)	$R_{\parallel}$ (mg/cm^2 Al)	ρ	$R_{\parallel}$ (mg/cm^2 Al)	ρ
109 ±0.3	0.47 ±0.02	0.58	0.48 ±0.02	0.60
104.5 ±0.3	0.70 ±0.03	0.44	0.73 ±0.03	0.42
99 ±0.3	0.70 ±0.02	0.42	0.74 ±0.03	0.39
94 ±0.3	0.91 ±0.04	0.36	0.93 ±0.04	0.28
91.5 ±0.3	0.92 ±0.04	0.32	0.94 ±0.04	0.25
89 ±0.3	0.97 ±0.04	0.28	0.95 ±0.04	0.36
87 ±0.3	1.02 ±0.04	0.26	0.98 ±0.04	0.21
84 ±0.3	0.94 ±0.04	0.25	0.94 ±0.04	0.27
79 ±0.3			1.02 ±0.04	

TABLE V. Experimental projected ranges $R_{\parallel}$ and range straggling ρ for ^{210}Po, ^{211}At, and ^{211}Rn produced through ^{40}Ar + ^{209}Bi reactions. The uncertainties in ρ values are of about ±15%.

	^{210}Po		^{211}At		^{211}Rn	
^{40}Ar E_{lab} (MeV)	$R_{\parallel}$ (mg/cm^2 Al)	ρ	$R_{\parallel}$ (mg/cm^2 Al)	ρ	$R_{\parallel}$ (mg/cm^2 Al)	ρ
294 ± 6			0.69 ± 0.04	0.49		
286 ± 7	0.71 ± 0.04	0.49	0.71 ± 0.04	0.49	0.69 ± 0.04	0.55
280 ± 8			0.79 ± 0.04	0.45		
272 ± 9	0.84 ± 0.04	0.42	0.83 ± 0.04	0.43	0.80 ± 0.04	0.53
265 ± 10			0.91 ± 0.04			
260 ± 7 [a]			0.89 ± 0.10	0.44	0.76 ± 0.10	0.45
249 ± 12			1.09 ± 0.06	0.37		
241 ± 9 [a]			1.07 ± 0.10	0.44	1.09 ± 0.10	0.53
236 ± 13	1.48 ± 0.07	0.26	1.30 ± 0.07	0.34	1.27 ± 0.07	0.44
233 ± 5 [a]			1.32 ± 0.10	0.32		
226 ± 11 [a]			1.63 ± 0.15	0.26		
223 ± 15			1.79 ± 0.09	0.23		
221 ± 7 [a]			1.50 ± 0.15	0.26	1.3 ± 0.2	0.24
217 ± 16	2.0 ± 0.1	0.23	1.9 ± 0.10	0.21	2.0 ± 0.1	0.31
215 ± 4			1.95 ± 0.10	0.31		
209 ± 17			2.3 ± 0.10	0.22		
207 ± 5			2.26 ± 0.11			
206 ± 9 [a]			2.15 ± 0.20	0.27		
203 ± 6			2.6 ± 0.10			
202 ± 4			2.14 ± 0.11	0.23	2.27 ± 0.11	0.21
201 ± 4			2.53 ± 0.12	0.17		
193 ± 5			2.87 ± 0.15	0.13		
192 ± 7			2.60 ± 0.13	0.15		
191 ± 19	2.84 ± 0.15	0.08	2.82 ± 0.15	0.11		
191 ± 7 [a]			3.10 ± 0.16			
190 ± 6			2.78 ± 0.14	0.19		
186 ± 8			2.93 ± 0.16			
182 ± 9			2.84 ± 0.14			
181 ± 7			2.94 ± 0.15	0.13		

[a] Data from Ref. 13 after correction (see text).

with those of ^{211}At and ^{210}Po will be discussed in Sec. IV.

Cross sections. The absolute cross sections obtained for the light and heavy reaction products at four energies (obtained with the device of Fig. 2) are given in Table X. The corresponding excitation functions are shown in Fig. 15. It is clear from Table X and Fig. 15 that the complementary products ^{39}Cl and ^{210}Po on one hand and ^{38}S and ^{211}At on the other hand are produced with the same cross sections in the energy range which has been explored (with a possible exception for ^{38}S and ^{211}At at low energy for which the difference in the cross sections exceeds slightly the calculated uncertainties).

IV. REACTIONS LEADING TO THE OBSERVED NUCLEI

As was already stated in previous papers on the same subject,[6-8] the identification of a final residue is not sufficient to specify unambiguously the nuclear reaction involved in its production. This is due to two factors: (i) the possible production of the observed nucleus from a radioactive parent, and (ii) the existence of many reaction channels leading to a given final product. For example, for ^{211}At production, one may consider the direct transfer of two protons from projectile to target followed by gamma deexcitation, a process denoted $(+2p,\gamma)$, the transfer of two protons and one neutron followed by one-neutron evaporation, a process denoted $(+2p+n,n)$, or more complex reaction paths.

In this section, an attempt will be made to specify more completely the reaction paths leading to the observed nuclei. Firstly, the question of the parent-daughter relationship will be studied. Secondly, the possible reaction paths will be tested by a kinematic analysis based on the angular and energetic distributions of heavy products. Finally, for Ar induced reactions, this study will be completed by using the results of the light product measurements.

TABLE VI. Same as Table V for $^{40}Ca + ^{209}Bi$ reactions.

	^{210}Po		^{211}At		^{211}Rn	
^{40}Ca E_{lab} (MeV)	$R_{\parallel}$ (mg/cm^2 Al)	ρ	$R_{\parallel}$ (mg/cm^2 Al)	ρ	$R_{\parallel}$ (mg/cm^2 Al)	ρ
275 ± 5	1.30 ± 0.06	0.31	1.17 ± 0.06	0.35	1.14 ± 0.06	0.38
249 ± 5	1.90 ± 0.09	0.22	1.66 ± 0.08	0.31	1.70 ± 0.08	0.31
226 ± 4	2.35 ± 0.12	0.20	2.17 ± 0.10	0.27	2.12 ± 0.10	0.19
225 ± 4	2.50 ± 0.12	0.19	2.37 ± 0.12	0.24	2.52 ± 0.12	0.17
218 ± 13	2.85 ± 0.14	0.18	2.79 ± 0.14	0.16	2.47 ± 0.13	
214 ± 4			2.94 ± 0.15	0.11	2.87 ± 0.15	0.10
213 ± 4	2.93 ± 0.15	0.15	3.04 ± 0.15	0.11	2.95 ± 0.15	0.15
211 ± 4			2.98 ± 0.15	0.13	2.97 ± 0.15	0.11
205 ± 7	3.05 ± 0.15	0.13	2.94 ± 0.15		2.98 ± 0.15	
204 ± 5			3.12 ± 0.16			
204 ± 5			2.91 ± 0.14			
202 ± 5			3.04 ± 0.15			
202 ± 6			2.94 ± 0.15	0.16		
199 ± 11			3.15 ± 0.16	0.16		
198 ± 6			3.06 ± 0.16	0.15		
197 ± 6			3.00 ± 0.15	0.15		
196 ± 3	3.20 ± 0.16	0.15	3.24 ± 0.16	0.09		
196 ± 3	2.93 ± 0.15	0.09	3.17 ± 0.16	0.10		
195 ± 8	3.00 ± 0.15	0.13	2.73 ± 0.14			
195 ± 6			2.80 ± 0.14			
193 ± 7			2.70 ± 0.14	0.17		
192 ± 7			2.84 ± 0.14	0.16		
187 ± 7	2.70 ± 0.14	0.20	2.69 ± 0.13	0.21		
186 ± 2	3.10 ± 0.16	0.19	2.85 ± 0.14	0.37		
180 ± 9			2.79 ± 0.14	0.21		

A. Decay of radioactive parents

The observed nuclei ^{210}Po and ^{211}At can either be produced directly or can result from the decay of radioactive parents, ^{210}Bi and ^{210}At for ^{210}Po, ^{215}Fr for ^{211}At. [The production of ^{211}At from the decay of ^{211}Rn ($T_{1/2} = 14.6$ h) is known from the decay-curve analysis and already subtracted.] For the incident ions and energies corresponding to the angular distributions measured here, the contributions of such precursors have been calculated, using the cross sections measured in Ref. 8. The

TABLE VII. Same as Table V for $^{56}Fe + ^{209}Bi$ reactions.

	^{210}Po		^{211}At		^{211}Rn	
^{56}Fe E_{lab} (MeV)	$R_{\parallel}$ (mg/cm^2 Al)	ρ	$R_{\parallel}$ (mg/cm^2 Al)	ρ	$R_{\parallel}$ (mg/cm^2 Al)	ρ
396 ± 8			1.73 ± 0.05	0.29		
371 ± 12			1.22 ± 0.07		1.34 ± 0.07	
328 ± 7	2.73 ± 0.14	0.30	2.80 ± 0.14	0.25	2.79 ± 0.14	0.26
317 ± 9	2.93 ± 0.15	0.20	3.08 ± 0.15	0.20	2.96 ± 0.15	0.22
308 ± 10	3.3 ± 0.2	0.26	3.4 ± 0.2	0.18	3.4 ± 0.2	0.19
304 ± 6	3.5 ± 0.2	0.18	3.5 ± 0.2	0.16	3.5 ± 0.2	0.17
298 ± 6			3.8 ± 0.2	0.17		
291 ± 7	3.9 ± 0.2	0.19	3.9 ± 0.2	0.16	4.0 ± 0.2	0.14
286 ± 8			4.2 ± 0.2	0.17		
284 ± 10	4.2 ± 0.2	0.15	4.1 ± 0.2	0.10		
282 ± 9			4.2 ± 0.2			
280 ± 8			4.1 ± 0.2	0.12		
276 ± 8	4.5 ± 0.2	0.05	4.2 ± 0.2	0.14		
273 ± 10			4.2 ± 0.2			
266 ± 10			4.1 ± 0.2			
266 ± 4			4.0 ± 0.2	0.18		
263 ± 11			4.3 ± 0.2			

TABLE VIII. Same as Table V for $^{63}Cu + ^{209}Bi$ reactions.

	^{210}Po		^{211}At		^{211}Rn	
^{63}Cu E_{lab} (MeV)	$R_{\parallel}$ (mg/cm^2 Al)	ρ	$R_{\parallel}$ (mg/cm^2 Al)	ρ	$R_{\parallel}$ (mg/cm^2 Al)	ρ
410 ± 9	2.4 ± 0.1	0.25	1.60 ± 0.08	0.30	1.64 ± 0.08	0.29
377 ± 8	2.9 ± 0.1	0.20	3.77 ± 0.07	0.19	3.6 ± 0.2	0.24
355 ± 11	3.7 ± 0.2	0.23	3.8 ± 0.2			
345 ± 7			4.0 ± 0.2	0.17		
338 ± 7			4.2 ± 0.2	0.14	4.3 ± 0.2	0.10
336 ± 8			4.5 ± 0.2	0.12		
328 ± 9			4.5 ± 0.2	0.11		
324 ± 9			4.8 ± 0.2	0.12		
321 ± 16	3.6 ± 0.2	0.28	4.6 ± 0.2	0.11	4.3 ± 0.2	0.13
321 ± 10			4.6 ± 0.2	0.10		
317 ± 10			4.8 ± 0.2	0.09	4.9 ± 0.2	0.09
309 ± 12			4.6 ± 0.2	0.10		
309 ± 2			4.9 ± 0.2	0.15		
305 ± 11			4.8 ± 0.2	0.23		
301 ± 13			4.3 ± 0.2	0.21		
295 ± 3			5.0 ± 0.2	0.12		

ratios $\sigma(^{210}At)/\sigma(210)$, $\sigma(^{210}Bi)/\sigma(210)$, and $\sigma(^{215}Fr)/\sigma(211)$, in which $\sigma(210)$ and $\sigma(211)$ denote the cumulative yields for ^{210}Po and ^{211}At, respectively, are given in Table XI. The value $\sigma(^{215}Fr)$, which is the cross section for the four-charge transfer reaction $^{40}Ar + ^{209}Bi \rightarrow ^{215}Fr$, has been taken equal to that for the similar reaction $^{40}Ar + ^{205}Tl \rightarrow ^{211}At$ measured in Ref. 8.

It can be seen from Table XI that the contributions of ^{210}Bi and ^{210}At, when measured, are always less than 25% of the observed ^{210}Po production. Therefore, the corresponding reactions have not been considered in the kinematic analysis. Similarly, the four-charge transfers have been neglected in the analysis concerning ^{211}At production through $^{40}Ar + Bi$ reactions, but they have been considered for the lighter projectiles ^{14}N, ^{16}O, ^{19}F.

As far as the light products from Ar induced reactions are concerned, the accumulation of cross sections due to β^- decays can be summarized by the following equations in which $\sigma(X)$ with $X = 43$, 41, 39, 38 denotes the measured cross sections for ^{43}K, ^{41}Ar, ^{39}Cl, and ^{38}S, respectively:

TABLE IX. Experimental projected ranges for ^{211}At produced through $^{40}Ar + Tl$ reactions.

$^{40}Ar + Tl$ E_{lab} (MeV)	^{211}At $R_{\parallel}$ (mg/cm^2 Al)
280 ± 8	0.96 ± 0.07
259 ± 7	1.07 ± 0.07
215 ± 4	2.05 ± 0.12
194 ± 5	2.5 ± 0.1

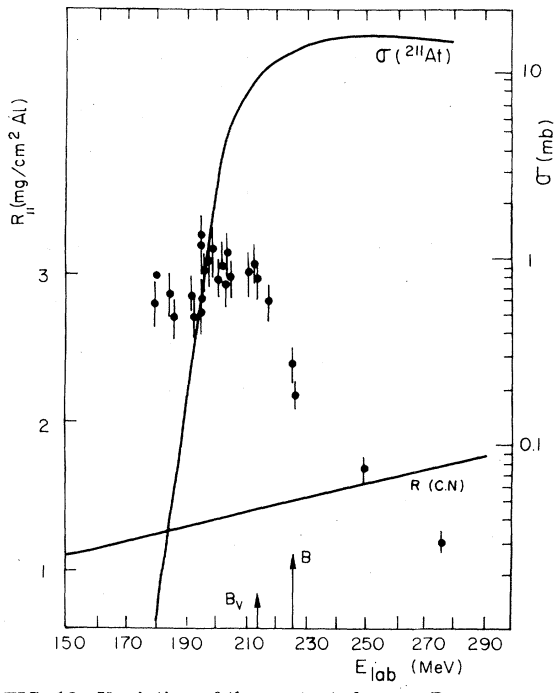

FIG. 12. Variation of the projected range $R_{\parallel}$ versus incident energy for the reaction $^{209}Bi + ^{40}Ca \rightarrow ^{211}At$. The experimental projected ranges are represented by the dots associated with error bars. The projected ranges calculated under the assumption of a compound nucleus process are represented by a curve labeled $R\,(CN)$. The excitation function for ^{211}At production is represented by the curve labeled $\sigma(^{211}At)$. The arrows labeled B and B_v indicate the interaction barriers calculated according to Ref. 19 and Ref. 24, respectively.

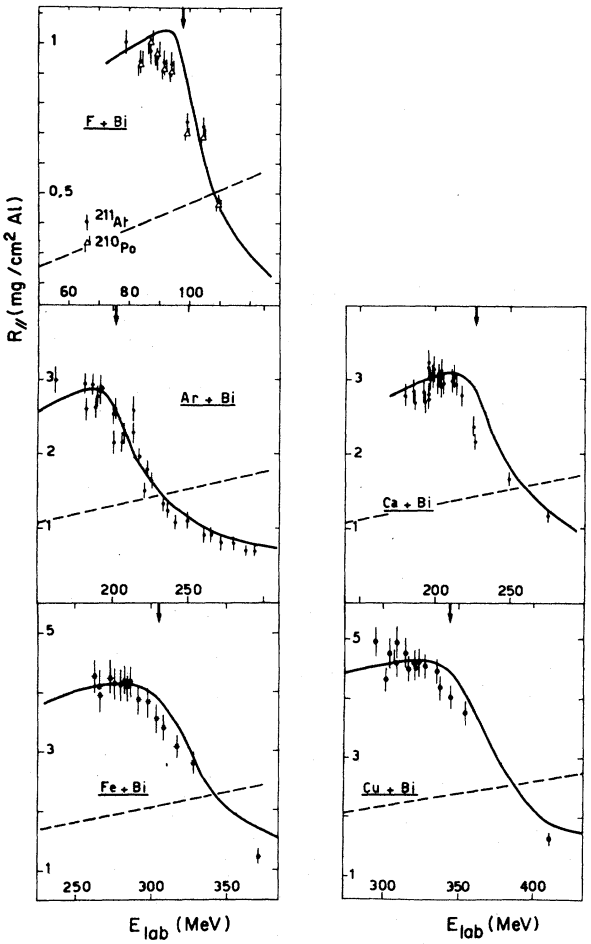

FIG. 13. Variation of the projected range $R_{\parallel}$ of the heavy products for reactions induced by ^{19}F, ^{40}Ar, ^{40}Ca, ^{56}Fe, and ^{63}Cu in ^{209}Bi. The arrows indicate the calculated strong interaction barriers as in Fig. 12. The solid lines are the ranges calculated for a two-proton transfer (see text). The dotted lines represent the ranges calculated under the assumption of a compound nucleus process.

$$\sigma(43) = \sigma(^{43}\mathrm{K}) + \underline{\sigma(^{43}\mathrm{Ar})} + \sigma(^{43}\mathrm{Cl}) + \cdots ,$$

$$\sigma(41) = \underline{\sigma(^{41}\mathrm{Ar})} + \sigma(^{41}\mathrm{Cl}) + \sigma(^{41}\mathrm{S}) + \cdots ,$$

$$\sigma(39) = \underline{\sigma(^{39}\mathrm{Cl})} + \sigma(^{39}\mathrm{S}) + \sigma(^{39}\mathrm{P}) + \cdots ,$$

$$\sigma(38) = \underline{\sigma(^{38}\mathrm{S})} + \sigma(^{38}\mathrm{P}) + \cdots .$$

In these equations, the term $\sigma(^{A}X)$ denotes the cross section for direct production of the isotope ^{A}X. For each line, the term which has been underlined is assumed to represent the main contribution to the observed cross section. This assumption is made because the corresponding reaction involves the transfer of the smallest number

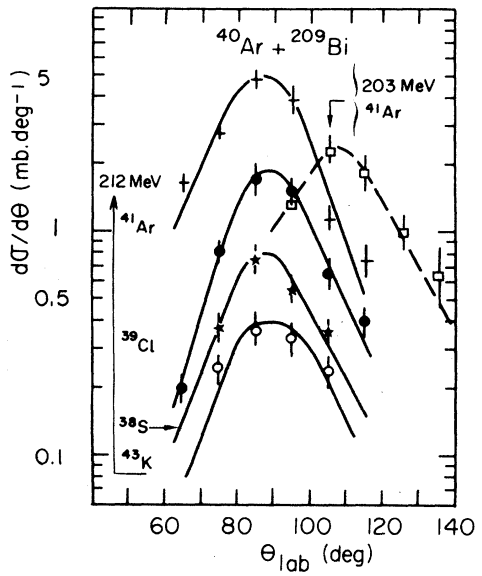

FIG. 14. Experimental angular distributions of light products from the reaction ^{40}Ar + ^{209}Bi. The lines are drawn to guide the eye.

of nucleons. Moreover, for $\sigma(43)$ the contribution of ^{43}K, produced by the transfer of one proton and two neutrons towards the projectile has been assumed to be smaller than that of ^{43}Ar produced by a three-neutron transfer. This hypothesis is based on the energetic balance $Q_{gg} - \Delta B$, which is more

TABLE X. Experimental cross sections for heavy and light products of Ar induced transfer reactions in ^{209}Bi. The complementary products (such as ^{211}At and ^{38}S) are found on the same horizontal line.

Energy E_{lab} (MeV)	Heavy product Isotope	σ (mb)	Light product Isotope	σ (mb)
212 ± 5	^{211}At	17 ± 3	^{38}S	17 ± 4
	^{210}At	12 ± 3		
	^{209}At	8 ± 2		
	^{210}Po	34 ± 9	^{39}Cl	36 ± 7
			^{41}Ar	106 ± 15
			^{43}K	11 ± 2
203 ± 5	^{211}At	15 ± 2	^{38}S	13 ± 4
	^{210}At	9 ± 3 [a]		
	^{210}Po	28 ± 7	^{39}Cl	27 ± 9
			^{41}Ar	75 ± 13
194 ± 5	^{211}At	7.5 ± 1	^{38}S	11 ± 2
	^{210}At	2 ± 0.5		
	^{209}At	0.9 ± 0.2		
	^{210}Po	23 ± 4	^{39}Cl	22 ± 5
			^{41}Ar	57 ± 8
190 ± 5	^{211}At	1.2 ± 0.15	^{38}S	1.9 ± 0.4
	^{210}At	<0.3 [a]		
	^{210}Po	5.7 ± 1.2	^{39}Cl	5 ± 1
			^{41}Ar	15 ± 2

[a] Estimated value.

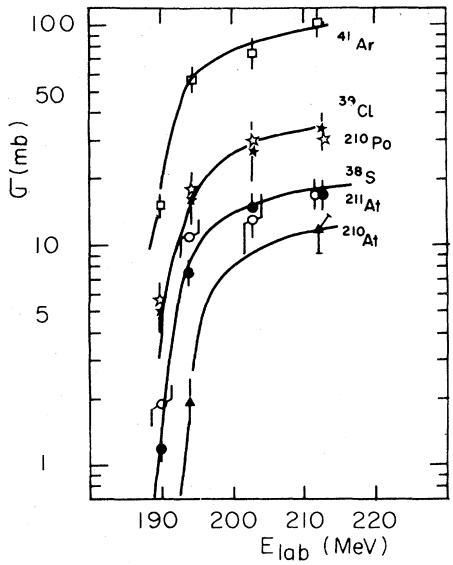

FIG. 15. Excitation functions for light and heavy products from the reaction $^{40}Ar + ^{209}Bi$. Open squares: ^{41}Ar; open stars: ^{39}Cl; black stars: ^{210}Po; open circles: ^{38}S; black circles: ^{211}At; black triangles: ^{210}At. The lines are drawn to guide the eye.

favorable to this last reaction (for this concept and for the notations, see Ref. 9). With these assumptions, the observation of ^{41}Ar, ^{43}K, ^{39}Cl, and ^{38}S correspond, respectively, to reactions in which one neutron, or three neutrons, or one proton, or two protons are transferred from projectile to target. It can be seen in Fig. 15 that the cross sections do decrease when the number of transferred particles is increased.

B. Kinematic analysis

The kinematic analysis has been performed on the basis of the ranges measured at each angle, as explained in Ref. 6, for all the reactions listed in Table XII, except for the reaction $^{19}F + Bi \rightarrow ^{210}Po$. For this reaction such ranges have not been measured accurately enough. Therefore, the analysis was made using the projected ranges, with the assumption that all the nuclei are emitted at the angle θ_{max} (known from the angular distribution). Let us recall that the principle of this analysis is to compare the kinetic energy measured for a given product to the maximal value which can be calculated under the assumption of a given mechanism. Such mechanisms are defined by specifying the nature and number of the particles transferred in the first reaction step and the associated excitation energy E^*. This energy must be such that the correct number of nucleons be evaporated in a second step to produce the observed nucleus. For example, the production of ^{211}At by the process denoted $(+2p, \gamma)$ corresponds to an ex-

TABLE XI. Contribution of the decay of radioactive parents to the production of the observed nuclei ^{210}Po and ^{211}At.

Ion	Energy (MeV)	$\frac{\sigma(^{210}At)}{\sigma(210)}$	$\frac{\sigma(^{210}Bi)}{\sigma(210)}$	$\frac{\sigma(^{215}Fr)}{\sigma(211)}$
^{14}N	74	<0.01	<0.02	
	99	<0.01	0.15	
^{16}O	83	0.01	<0.02	
	102	0.25	<0.03	
^{19}F	95	<0.01		
	110	0.1		
^{40}Ar	203	0.20		~0.1
	212	0.23		~0.1
	275	0.25		~0.1

TABLE XII. Most probable reaction path leading to the observed heavy products ^{210}Po, ^{211}At, and ^{211}Rn.

Ion	Energy (MeV)	E/B	Most probable reaction path ^{210}Po	^{211}At	^{211}Rn
^{14}N	74	1.01	$(+p,\gamma)$	$(+2p,\gamma)$	$(+^{14}N, 4n)$ [a]
	99	1.34	$(+p,\gamma), (+p+n,n)$	$(+2p,\gamma), (+2p+n,n)$ $(+2p+2n,2n)$	$(+^{14}N, \alpha 4n)$ [a], $(+3p,n)$ [b]
^{16}O	83	1.0	$(+p,\gamma), (+p+n,n)$	$(+2p,\gamma)$	
	102	1.21	$(+p,\gamma), (+p+n,n)$	$(+2p,\gamma), (+2p+n,n)$ $(+^{8}Be, 2n)$ [c], $(+^{12}C, \alpha 2n)$ [c]	
^{19}F	95	0.99	$(+p,\gamma), (+p+n,n)$	$(+2p,\gamma)$	
	110	1.15	$(+p,\gamma), (+p+n,n)$	$(+2p,\gamma), (+2p+n,n)$	
^{40}Ar	203	1.0	$(+p,\gamma)$ [d]	$(+2p,\gamma)$ [d]	
	275	1.36	$(+p,\gamma), (+p+n,n)$	two-charge transfer	
^{40}Ca	217	0.96		two-charge transfer	three-charge transfer

[a] Compound nucleus process.
[b] For the shoulder at 40° (see Fig. 3).
[c] For the shoulder at 15–20° (see Fig. 4).
[d] From the measurements of light products (Sec. III C).

citation energy E_0^* less than the neutron binding energy (8 MeV), while the process denoted $(+2p+n,n)$ involves an excitation energy E_1^* of ^{212}At such that 8 MeV $< E_1^* <$ 15 MeV. This excitation energy E_1^* ensures the evaporation of one neutron. The maximum kinetic energy of the residue is associated to the lowest limit for E^* and corresponds to a cold light reaction product. The processes for which this maximum energy is lower than the measured value can be excluded without ambiguity.

The most probable reaction paths resulting from the analysis are given in Table XII. Several comments can be made relative to these results.

Firstly, except for ^{211}Rn production through ^{14}N induced reactions, which is due to a compound nucleus process at both energies, all the angular distributions correspond to transfer reactions.

Secondly, for 102 MeV ^{16}O ions, the shoulder observed at $\theta = 15°$ in the ^{211}At angular distribution can be explained by a four-charge (or six-charge) transfer. It is interesting to note that such a transfer of two α particles (or a ^{8}Be nucleus) was observed with a much higher probability in ^{12}C induced reactions,[6] while it is not observed for ^{14}N and ^{19}F ions. This can be interpreted as an effect of the projectile structure.

Thirdly, for ^{211}At production with light ions at the barrier energy, the only reaction path which is not excluded is the $(+2p,\gamma)$ process, i.e., the least energy consuming. This is due to the dramatic influence of the energetics on the transfer probability, which has been outlined several times.[8,10,27] When the incident energy is increased, the process $(+2p+n,n)$, which requires more energy, becomes possible. A similar behavior seems to be observed, but less clearly, for one-charge transfer reactions. These conclusions confirm the indications obtained in the early work of Croft *et al.*[25] on the same subject.

Finally, for ^{40}Ar and ^{40}Ca ions, the kinematic analysis is not precise enough to determine the number of neutrons transferred together with one proton (for ^{210}Po) or two protons (for ^{211}At). However, for incident ^{40}Ar ions, the production of these isotopes can be assigned to the processes $(+p,\gamma)$ and $(+2p,\gamma)$, respectively. Such an assignment is made on the basis of the light fragment study (similarity of the shape and amplitude of the excitation functions and complementarity of the angular distributions for the complementary residues ^{39}Cl and ^{210}Po on one hand and ^{38}S and ^{211}At on the other hand). From the above mentioned energetics arguments, one may think that these processes $(+p,\gamma)$ and $(+2p,\gamma)$ are also predominant for ^{210}Po and ^{211}At production, at least at low energy, for the heaviest projectiles ^{40}Ca, ^{56}Fe, and ^{63}Cu.

V. INTERPRETATION

A. Angular and energetic distributions of heavy residues in the c.m. system

From the laboratory angular distributions and the ranges measured at all angles θ_{lab} for the heavy reaction products, it is possible to get the angular and energetic distributions of these products in the c.m. system. This laboratory to c.m. transformation is made using the method described in Ref. 28. Examples of the c.m. distributions are given in Figs. 16–18 for the reactions

$$^{14}\mathrm{N} + {}^{209}\mathrm{Bi} \rightarrow {}^{211}\mathrm{At} \text{ at 74 and 99 MeV},$$

and

$$^{40}\mathrm{Ar} + {}^{209}\mathrm{Bi} \rightarrow {}^{211}\mathrm{At} \text{ at 212 and 275 MeV}.$$

In Figs. 16–18 are shown the c.m. angular distributions, energy distributions, and the contour plots which represent the variation of the double differential cross section versus angle and energy. Except for those relative to Ar induced reactions at 275 MeV, all the curves exhibit the shape typical of quasi-elastic transfer, with a single peak in the angular and energy distributions, and a limited extension in the $(\bar{\theta},\bar{E})$ plane. The position of the peak in the angular distribution is always close to the grazing angle, calculated for the heavy product using the relation

$$\bar{\theta}_{gr} = \pi - 2\arcsin\left[\frac{2r_0(A_p^{1/3}+A_t^{1/3})\ A_t E_p}{Z_p Z_t e^2 (A_t + A_p)} - 1\right]^{-1} \quad (4)$$

with $r_0 = 1.5$ fm for ^{14}N ions, and 1.45 fm for ^{40}Ar ions,[11] and indicated by an arrow in Figs. 16–18. In Eq. (4), A_t and Z_t denote the target mass and charge, and E_p is the laboratory projectile energy.

The distributions relative to ^{40}Ar induced reactions at 275 MeV differ from the previous ones (see the two-dimensional diagram in Fig. 18). In addition to the quasi-elastic peak ($\bar{\theta} = 110°$, $\bar{E} \sim 35$ MeV), they exhibit a tail towards lower energies and larger angles. Such a tail is typical of partially damped events in deeply inelastic reactions.[5,26] Therefore, for such high-energy incident Ar ions, the total production of ^{211}At cannot be assigned any more to quasi-elastic processes. One should particularly note in Fig. 18 that the most probable energy (maximum in the $d\sigma/d\bar{E}$ distribution) is now different from the quasi-elastic energy (maximum in the $d^2\sigma/d\bar{\theta}d\bar{E}$ distribution).

The kinematic analysis used in Sec. IV to identify the reactions leading to the observed isotopes can obviously be made in the c.m. system. The limits of c.m. energy calculated for three types of transfer are indicated in Figs. 16–18. The comparison of these limits with the experimental energy distributions leads us to the same conclu-

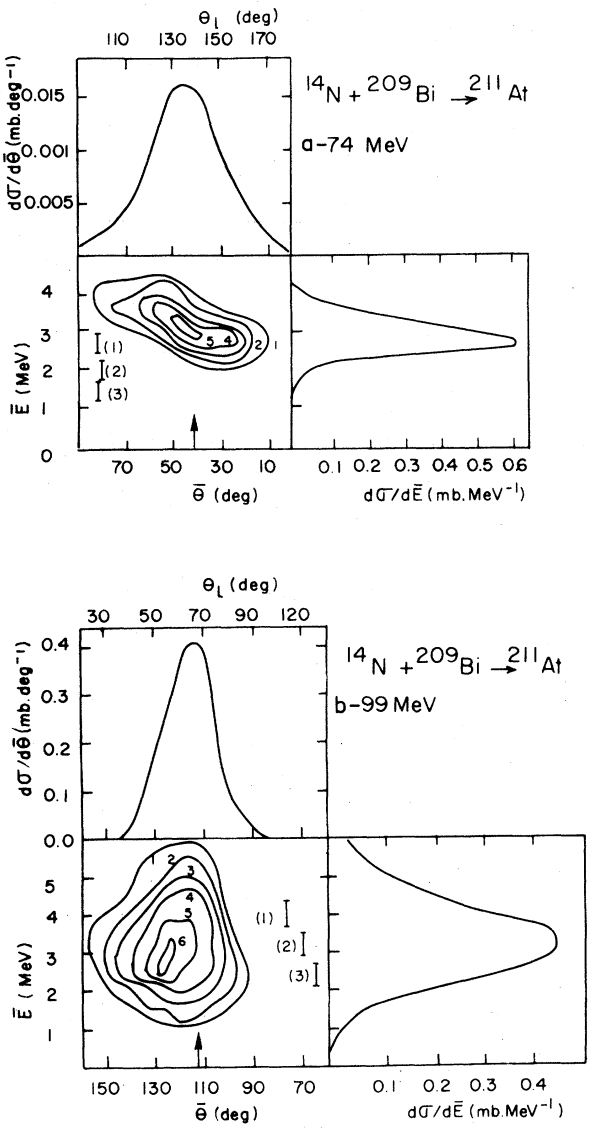

FIG. 16. Angular and energy distributions of ^{211}At produced through ^{14}N + ^{209}Bi reactions (a) at E_{lab} = 74 MeV and (b) at E_{lab} = 99 MeV. The scaling relative to heavy product angles $\bar{\theta}$ has been made from the right to the left in order to make easier the comparison with data concerning light fragments. The upper scale $\bar{\theta}_l = 180° - \bar{\theta}$ is relative to the associated light product. The contour plots represent lines of equal double differential cross section $d^2\sigma/d\bar{\theta}d\bar{E}$ (expressed in arbitrary units by the number written close to each line). The vertical bars labeled (1), (2), (3) represent the calculated energies for the processes $(+2p,\gamma)$, $(+2p+n,n)$, and $(+2p+2n,2n)$, respectively.

sions as in Sec. IV; for ^{14}N + Bi at 74 MeV, only the process $(+2p,\gamma)$ is consistent with the measured energy. For the same reaction at 99 MeV, the energy distribution is broader and the three processes considered are possible.

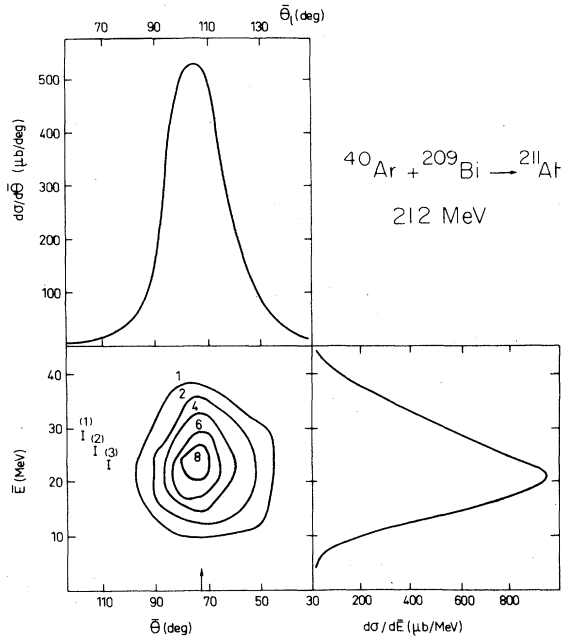

FIG. 17. Same as Fig. 16 for ^{40}Ar induced reactions at E_{lab} = 212 MeV.

For 212 MeV Ar projectiles, the experimental precision is not sufficient to distinguish among the three reaction paths considered, all of them being inside the FWHM of the distribution. Finally, for 275 MeV Ar ions, these reaction paths can explain the "quasi-elastic" peak, but not the tail corresponding to partially damped events. To explain

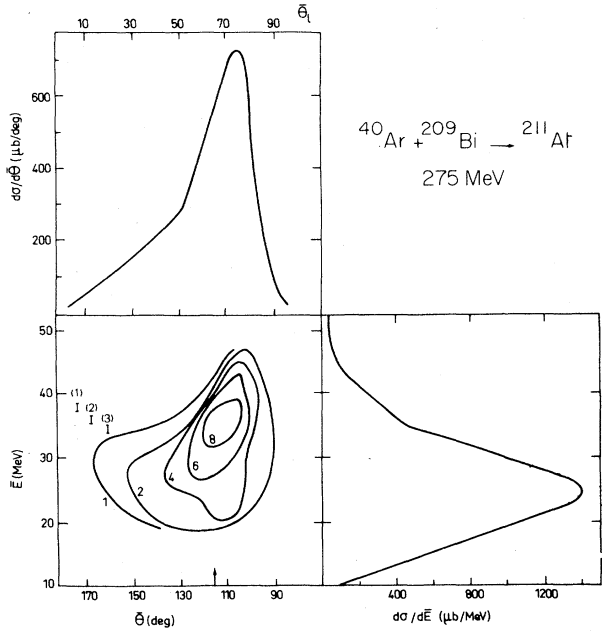

FIG. 18. Same as Fig. 16 for ^{40}Ar induced reactions at E_{lab} = 275 MeV.

the low kinetic energies associated with these events, one should invoke reactions in which substantial amounts of excitation energy would be given to both projectile and target, i.e., a large number of particles would be evaporated. However, the low cross section measured for the four-charge transfer reaction $^{40}Ar + ^{205}Tl \rightarrow ^{211}At$ at the same energy seems to indicate that most of the ^{211}At production must be assigned to two-charge transfer (quasi-elastic + deeply inelastic transfer).

Each angular distribution can be defined by the position of its maximum $\overline{\theta}_{max}$ and its full width at half maximum. These parameters, which have been derived from Gaussian fits to the distributions, are given in Table XIII for all the systems studied. The value of $\overline{\theta}_{max}$ depends mainly on the ratio E/B, and this point will be discussed in Sec. V C. The values of $\overline{\theta}_{max}$ and FWHM have been used in Ref. 11 for a quantitative analysis of the data. This analysis was made using a formalism derived from a general treatment of multinucleon transfer,[29] in an approach similar to that of Frahn and Venter[30] for neutron transfer reactions, i.e., in the limits of the distorted wave Born approximation. It led to the determination of the optimal distance of closest approach for the transfer reactions considered. The whole set of data was consistent with an interaction distance $d = 2.7$–3 fm between the half-density radii of the colliding nuclei. This d value is in good agreement with the distances deduced from elastic scattering analysis by Schröder and Huizenga.[31]

B. Correlation between heavy and light fragment distributions for ^{40}Ar induced reactions

For ^{40}Ar induced reactions, at an incident energy of 212 MeV, the laboratory angular distributions of ^{210}Po and ^{211}At exhibit a maximum for $\theta_{max} = 35 \pm 5°$. (See Fig. 6.) If one makes the assumption that these nuclei are produced through the processes $(+p, \gamma)$ and $(+2p, \gamma)$, respectively, the corresponding light fragments are ^{39}Cl and ^{38}S. In order to satisfy the momentum and energy conservation laws, these fragments should be emitted at the "complementary" angles $\theta'_{max}(^{39}Cl) = 96 \pm 10°$ and $\theta'_{max}(^{38}S) = 95 \pm 10°$ in the laboratory system. These calculated angles are in fair agreement with the experimental maxima observed at $88 \pm 5°$ for both distributions (see Fig. 14). Moreover, the kinetic energy calculated for ^{211}At under the same assumption is equal to 68 ± 7 MeV, i.e., very close to the measured value $E_R = 73 \pm 14$ MeV (see Table II). These numbers, together with the similarities observed between the excitation functions relative to complementary products (see Fig. 15), are a good confirmation of the inferred mechanisms.

TABLE XIII. Parameters $\overline{\theta}_{max}$ and FWHM defining the position and width of the angular distributions in the c.m. system.

Reaction	E_{lab} (MeV)	$\overline{\theta}_{max}$ (deg)	FWHM (deg)
$^{14}N + ^{209}Bi \rightarrow ^{210}Po$	74	56	40
	99	120	22
$^{14}N + ^{209}Bi \rightarrow ^{211}At$	74	48	36
	99	118	32
$^{16}O + ^{209}Bi \rightarrow ^{211}At$	83	46	40
	102	105	22
$^{19}F + ^{209}Bi \rightarrow ^{211}At$	95	44	36
	110	96	20
$^{40}Ar + ^{209}Bi \rightarrow ^{211}At$	203	50	32
	212	76	17
	275	120	14
$^{40}Ca + ^{209}Bi \rightarrow ^{211}At$	217	46	32

C. Influence of the ratio E/B on the angular distributions and correlation with the rainbow angle

As was already outlined in Sec. III, for the data in the laboratory system, the angular distributions seem to be strongly influenced by the ratio E/B of the incident energy over the interaction barrier. This is particularly clear in Fig. 19, where the angle $\overline{\theta}_{max}$ relative to two-charge transfers has been plotted versus E/B, for all the systems studied. A strong correlation is observed between $\overline{\theta}_{max}$ and E/B for all projectiles. This property is similar to that mentioned by da Silveira[32] concerning the rainbow angle $\overline{\theta}_r$ in elastic scattering. Therefore, it is interesting to compare the variation of $\overline{\theta}_{max}$ and $\overline{\theta}_r$ versus E/B. Such a comparison is shown in Fig. 19. The solid line represents the variation $\overline{\theta}_r = f(E/B)$ calculated in Ref. 32 using a Woods-Saxon nuclear potential. In order to verify that the shape of this potential does not influence the value of $\overline{\theta}_r$, provided that the height of the interaction barrier is respected, we have calculated some values of $\overline{\theta}_r$ using a nuclear potential derived from the energy density formalism.[19] These values are represented by triangles in Fig. 19, and one can see that they agree perfectly with the solid curve.

A striking similarity is observed between the curves $\overline{\theta}_{max} = f(E/B)$ and $\overline{\theta}_r = f(E/B)$, the former being slightly shifted towards low values of E/B relative to the latter. If one remembers that the calculated curve was in good agreement with the observed maxima for angular distributions relative to neutron transfer,[20] the shift observed here (which corresponds to a preferential emission of the light product at smaller angles) can be attributed to an effect of the charge transfer, which decreases the projectile charge by two units, i.e.,

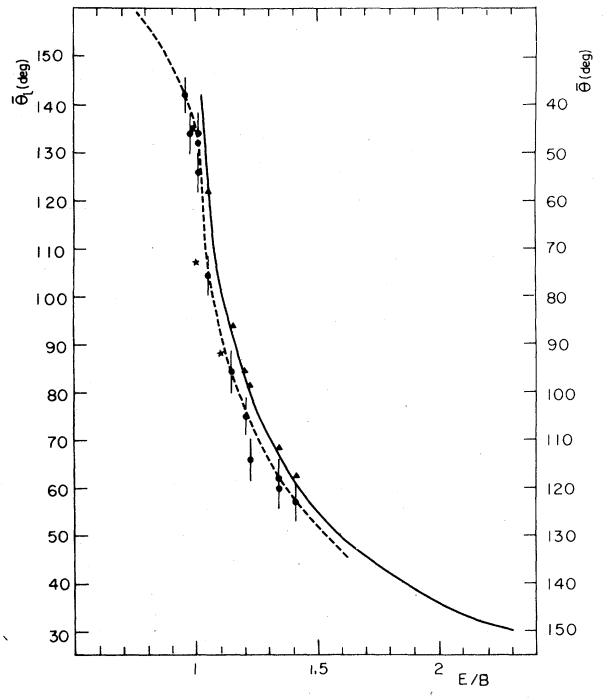

FIG. 19. Variation of $\bar{\theta}_{max}$ and of the rainbow angle $\bar{\theta}_r$ versus the ratio E/B. The angle $\bar{\theta}_r$ is calculated with (i) a Woods-Saxon potential (Ref. 32): solid line; (ii) a potential derived from the energy density formalism (Ref. 19): triangles. The points associated with error bars represent the experimental values of $\bar{\theta}_{max}$ relative to two-proton transfer for all projectiles but ^{40}Ca. The stars represent the same data for ^{40}Ca projectiles. The dotted line has been drawn through the experimental points and arbitrarily extrapolated at low energy.

reduces its deviation by the Coulomb field. (Note that this shift would be somewhat reduced by using strong interaction barriers from Ref. 24.) The vicinity of the two curves may thus be interpreted as an indication that the transfer reactions take place for distances of closest approach close to those corresponding to the rainbow effect. This is confirmed by the quantitative analysis made in Ref. 11, and this result is in good agreement with the conclusions of Ref. 33. Moreover, the data shown in Fig. 19 may be used to predict the position of the angular distribution maximum, in the c.m. system for one- and two-proton transfer reactions.

Let us note, finally, that the laboratory rainbow angle θ_r relative to the heavy partner of the collision can easily be calculated from the c.m. value $\bar{\theta}_r$ using the well known relation

$$\theta_r = \bar{\theta}_r/2 \tag{5}$$

This relation is valid for elastic scattering and for the nucleus initially at rest in the laboratory frame. The curve $\theta_r = f(E/B)$ obtained from this transformation is shown in Fig. 10, and gives an explanation for the correlation observed in Sec. III between θ_{max} and E/B, for $a/A_p < 0.2$. This correlation is the result of the nearly equal values of $\bar{\theta}_{max}$ and $\bar{\theta}_r$, associated to the quasi-elastic nature of the collision, which makes it possible to use the relation $\theta_{max} \simeq \bar{\theta}_{max}/2$, when the ratio a/A_p is sufficiently low. When this ratio increases, even if $\bar{\theta}_{max}$ does not deviate strongly from θ_r, the c.m. to laboratory transformation does not correspond any more to Eq. (5), and this explains the deviations observed between θ_{max} and θ_r for $a/A_p \geq 0.2$ [see Fig. 10(b)].

D. Variation of projected ranges with incident energy

The general behavior observed in Figs. 12 and 13 for the variation of projected ranges with incident energy, can be explained in the following way:

At low incident energies, the distance of closest approach of the nuclei is limited by Coulomb repulsion, and only the head-on collisions can lead to transfer reactions. This implies that the projectile residue be emitted backwards, and the target residue at small angle (in the laboratory system), with a velocity well above that which corresponds to total momentum transfer. When the incident energy is increased, but remains lower than the strong interaction barrier, the nuclei come into closer contact and the transfer probability is increased. However, the emission angle of the heavy fragment remains small, and its velocity increases (effect of the momentum conservation), so that the projected range increases. Finally, when the incident energy exceeds the strong interaction barrier, the head-on collisions lead to fusion, or deeply inelastic reactions, and the transfer reactions are governed by the well known rule of the constant distance of approach.[34] This implies a decrease of the laboratory kinetic energy of the heavy residue, associated with an increase of its emission angle. Both phenomena lead to the decreasing behavior observed for the projected range at high energy.

The evolution of the projected ranges with increasing incident energies is consistent with the above mentioned variation of $\bar{\theta}_{max}$ versus E/B. This can be verified in the following way: For a given projectile and energy, the angle $\bar{\theta}_{max}$ is determined using the dotted line in Fig. 19. This line has been drawn through the experimental points with an arbitrary extrapolation at low energy. (The exact position of the curve for these low energies has little influence on the projected ranges calculated as explained below.) The c.m. energy of products $\bar{E}$ is calculated assuming a $(+p,\gamma)$ or a $(+2p,\gamma)$ process. From $\bar{\theta}_{max}$ and $\bar{E}$, the laboratory angle θ_{max} and energy E can be calculated, and

the laboratory energy is converted into recoil range $R(\theta_{max})$ according to the relation represented by the curve in Fig. 11. Then the mean projected range $R_{\parallel}$ is calculated by the relation

$$R_{\parallel} = R(\theta_{max})\cos\theta_{max} . \quad (6)$$

The results of such calculations are represented by solid lines in Fig. 2. These curves are sensitive to the value adopted for the barrier B (indicated by arrows in Fig. 13). For example, for the Ca + Bi system, a change of less than 5% in B would remove the difference between the curve and the experimental points. Taking this remark into account, the agreement with the experiment is surprisingly good. As far as ^{56}Fe and ^{63}Cu projectiles are concerned, this agreement is a good indication that the variation of $\bar{\theta}_{max}$ with E/B (for which no direct measurement has been made) can be taken from Fig. 19, i.e., is the same as for lighter projectiles.

VI. CONCLUSION

Recoil techniques have been used to measure the angular distributions and ranges of ^{210}Po, ^{211}At, and ^{211}Rn produced through heavy ion reactions with ^{209}Bi. These reactions involved the transfer of one, two, and three protons, respectively. The projectiles ranged from ^{14}N to ^{63}Cu. The results obtained indicate a great unity in the characteristics of quasi-elastic transfer reactions for all the projectiles.

At low incident energy, the reaction path which leads to the formation of the observed nucleus is always that which corresponds to the minimal energy cost. This confirms the strong influence of the reaction energetics on the transfer probability, which was previously observed in the study of the excitation function thresholds.[8,10] At higher energies, more complex reaction channels take place with significant probabilities.

The position of the angular distribution maxima, in the laboratory and c.m. frames, are strongly correlated with the ratio E/B of the incident energy to the interaction barrier. The corresponding curves are independent of the projectile and of the nature of the transferred particles if the ratio of the transferred mass a to the projectile mass A_p is low enough ($a/A_p < 0.2$). This property can be used to predict the position of the angular distribution maximum for other transfer reactions. Moreover, the correlation appears to be very similar to that of the rainbow angle with the ratio E/B. This indicates a strong influence of the rainbow effect on the angular distribution for quasi-elastic transfer, and can be taken as an indication that the distances of closest approach corresponding to maximal transfer probabilities are not far from those corresponding to the rainbow effect. This conclusion is in agreement with the quantitative analysis of these data,[11] and with the study made by Vaz *et al.*[33] on ^{16}O + ^{208}Pb reactions.

We thank the crews of the Orsay heavy ion accelerators (ALICE and MP Tandem) for their cooperation, L. de Reilhac for helping in some of the experiments, and J. M. Alexander for a critical reading of the manuscript.

[1] J. Galin, D. Guerreau, M. Lefort, J. Péter, X. Tarrago, and R. Basile, Nucl. Phys. A159, 461 (1970).
[2] J. L. C. Ford Jr., K. S. Toth, G. R. Satchler, D. C. Hensley, L. W. Owen, R. M. DeVries, R. M. Gaedke, P. J. Riley, and S. T. Thornton, Phys. Rev. C 10, 1429 (1974).
[3] C. Olmer, M. Mermaz, M. Buenerd, C. K. Gelbke, D. L. Hendrie, J. Mahoney, D. K. Scott, M. M. MacFarlane, and S. C. Pieper, Phys. Rev. C 18, 205 (1978).
[4] M. C. Lemaire, Phys. Rep. 7C, 279 (1973).
[5] A. Fleury and J. M. Alexander, Annu. Rev. Nucl. Sci. 24, 279 (1974).
[6] R. Bimbot, D. Gardès, and M. F. Rivet, Nucl. Phys. A189, 193 (1972).
[7] R. Bimbot and M. F. Rivet, Phys. Rev. C 8, 375 (1973).
[8] D. Gardès, R. Bimbot, J. Maison, L. de Reilhac, M. F. Rivet, A. Fleury, F. Hubert, and Y. Llabador, Phys. Rev. C 18, 1298 (1978).
[9] D. Gardès, R. Bimbot, A. Fleury, F. Hubert, and M. F. Rivet, J. Phys. Lett. 36, 59 (1975).
[10] R. Bimbot, D. Gardès, J. Cugnon, and R. da Silveira, Z. Phys. A290, 157 (1979).
[11] Y. Llabador, F. Hubert, A. Fleury, D. Gardès, M. F. Rivet, and R. Bimbot, Z. Phys. A289, 173 (1979).
[12] R. Bimbot, C. Cabot, J. Depauw, D. Gardès, H. Gauvin, L. Martial, A. Richomme, and M. F. Rivet, Report No. IPNO-RC-79-03 (unpublished).
[13] R. Bimbot, D. Gardès, and M. F. Rivet, Phys. Rev. C 4, 2180 (1971).
[14] J. M. Alexander, in *Nuclear Chemistry*, edited by L. Yaffe (Academic, New York, 1968).
[15] R. Bimbot, D. Gardès, R. L. Hahn, Y. de Moras, and M. F. Rivet, Nucl. Phys. A228, 85 (1974); and A248, 377 (1975).
[16] R. Bimbot and D. Gardès, Nucl. Instrum. Methods 109, 333 (1973).
[17] J. M. Alexander and G. N. Simonoff, Phys. Rev. 133, B93 (1964).
[18] C. M. Lederer and V. S. Shirley, *Table of Isotopes*, VIIth edition (Wiley, New York, 1978).
[19] C. Ngô, B. Tamain, J. Galin, M. Beiner, and R. J. Lombard, Nucl. Phys. A240, 353 (1975).
[20] J. M. Alexander and L. Winsberg, Phys. Rev. 121, 529 (1961).
[21] L. Winsberg and J. M. Alexander, Phys. Rev. 121,

518 (1961).
[22]P. M. Strudler, I. L. Preiss, and R. Wolfgang, Phys. Rev. 154, 1126 (1967).
[23]L. C. Northcliffe and R. F. Schilling, Nucl. Data Tables A7, 233 (1970).
[24]L. C. Vaz and J. M. Alexander, Phys. Rev. C 10, 464 (1974).
[25]P. D. Croft, J. M. Alexander, and K. Street, Phys. Rev. 165, 1380 (1968).
[26]F. Hubert, H. Delagrange, and A. Fleury, Nucl. Phys. A228, 415 (1974).
[27]R. M. Diamond, A. M. Poskanzer, F. S. Stephens, W. J. Swiatecki, and D. Ward, Phys. Rev. Lett. 20, 802 (1968).
[28]M. F. Rivet, R. Bimbot, A. Fleury, D. Gardès, and Y. Llabador, Nucl. Phys. A276, 157 (1977).
[29]C. Toeppfer, Z. Phys. 253, 78 (1972).
[30]W. E. Frahn and R. H. Venter, Nucl. Phys. 59, 651 (1964).
[31]W. V. Schröder and J. R. Huizenga, Annu. Rev. Nucl. Sci. 27, 465 (1977).
[32]R. da Silveira, Phys. Lett. 50B, 237 (1974).
[33]L. C. Vaz, J. M. Alexander, and E. M. Auerbach, Phys. Rev. C 18, 820 (1978).
[34]J. A. McIntyre, T. L. Watts, and F. C. Jobes, Phys. Rev. 119, 1331 (1960).